RAA 2021 Vol. **21** No. **12**, 318(19pp) doi: 10.1088/1674-4527/21/12/318

http://www.raa-journal.org *http://iopscience.iop.org/raa*

***R**esearch in*
***A**stronomy and*
***A**strophysics*

Investigation of two coronal mass ejections from circular ribbon source region: Origin, Sun-Earth propagation and Geoeffectiveness

M. Syed Ibrahim[1,2], Wahab Uddin[1], Bhuwan Joshi[3], Ramesh Chandra[4] and Arun Kumar Awasthi[5]

[1] Aryabhatta Research Institute of Observational Sciences, Nainital 263002, India; *syed.ibrahim@iiap.res.in*
[2] Kodaikanal Solar Observatory, Indian Institute of Astrophysics, Kodaikanal-624103, Tamil Nadu, India
[3] Udaipur Solar Observatory, Physical Research Laboratory, Udaipur 313004, India
[4] Department of Physics, DSB Campus, Kumaun University, Nainital 263002, India
[5] CAS Key Laboratory of Geospace Environment, Department of Geophysics and Planetary Sciences, University of Science and Technology of China, Hefei 230026, China

Received 2021 April 7; accepted 2021 September 22

Abstract In this article, we compare the properties of two coronal mass ejections (CMEs) that show similar source region characteristics but different evolutionary behaviors in the later phases. We discuss the two events in terms of their near-Sun characteristics, interplanetary evolution and geoeffectiveness. We carefully analyzed the initiation and propagation parameters of these events to establish the precise CME-interplanetary CME (ICME) connection and their near-Earth consequences. The first event is associated with poor geomagnetic storm disturbance index (Dst ≈-20 nT) while the second event is associated with an intense geomagnetic storm of DST ≈-119 nT. The configuration of the sunspots in the active regions and their evolution are observed by Helioseismic and Magnetic Imager (HMI). For source region imaging, we rely on data obtained from Atmospheric Imaging Assembly (AIA) on board Solar Dynamics Observatory (SDO) and Hα filtergrams from the Solar Tower Telescope at Aryabhatta Research Institute of Observational Sciences (ARIES). For both the CMEs, flux rope eruptions from the source region triggered flares of similar intensities (≈M1). At the solar source region of the eruptions, we observed a circular ribbon flare (CRF) for both cases, suggesting fan-spine magnetic configuration in the active region corona. The multi-channel SDO observations confirm that the eruptive flares and subsequent CMEs were intimately related to the filament eruption. Within the Large Angle and Spectrometric Coronograph (LASCO) field of view (FOV) the two CMEs propagated with linear speeds of 671 and 631 km s^{-1}, respectively. These CMEs were tracked up to the Earth by Solar Terrestrial Relations Observatory (STEREO) instruments. We find that the source region evolution of CMEs, guided by the large-scale coronal magnetic field configuration, along with near-Sun propagation characteristics, such as CME-CME interactions, played important roles in deciding the evolution of CMEs in the interplanetary medium and subsequently their geoeffectiveness.

Key words: Sun: coronal mass ejections (CMEs) — Sun: flares

1 INTRODUCTION

Flares and coronal mass ejections (CMEs) are the largest eruptive phenomena in our solar system. Flares are characterized by a sudden catastrophic release of energy in the solar atmosphere. A huge amount of energy (in excess of 10^{32} erg) is released within a few minutes (see review by Benz 2017). The standard flare model provides a basic framework to understand the relationship between solar flares and filament eruptions (see e.g., Carmichael 1964; Sturrock 1966; Hirayama 1974; Kopp & Pneuman 1976).

In the standard flare model, the expansion of a filament from the core of the active region (AR) forms an integral part of the triggering process of an eruptive flare (Shibata 1999; Joshi et al. 2012). Filaments are the large magnetic structures which are capable of storing magnetic energy to drive the eruptions (see e.g., Gibson & Fan 2006; Krall & Sterling 2007; Uddin et al. 2012; Mitra et al. 2018). The overlying AR magnetic loops are stretched by the filament eruption and the magnetic reconnection sets in underneath the erupting filament. The accelerated particles precipitate along the newly formed post-reconnected

field lines and subsequently produce bright flare ribbons in the chromosphere (see e.g., Demoulin et al. 1996; Joshi et al. 2015, 2017b). Flare ribbons are observed in various geometric shapes like parallel, J-shaped, X-shaped, circular and multi-ribbons (see e.g., Janvier et al. 2016; Li et al. 2016; Masson et al. 2009; Reid et al. 2012; Kushwaha et al. 2014; Joshi et al. 2017a; Zhong et al. 2019; Toriumi & Wang 2019; Devi et al. 2020; Liu et al. 2020). Chromospheric flare ribbons are generally situated at locations intersected by separatrices dividing domains of distinct connectivity or quasi-separatrix layers possessing strong connectivity gradients (Hudson 2011). Magnetic field lines associated with a three-dimensional (3D) coronal null point usually display a fan-spine configuration, where the dome-shaped fan portrays the closed separatrix surface and the inner and outer spine field lines in different connectivity domains pass through the null point (Démoulin et al. 1994; Demoulin et al. 1997). The footpoint of the inner spine has a magnetic polarity opposite to those of the fan, which forms a circular polarity inversion line (Lau & Finn 1990; Aulanier et al. 2005). Magnetic reconnection can be induced in such single null points, as the fan/spines deviate from the null when subject to shearing or rotational perturbations (Pontin et al. 2007; Pontin & Galsgaard 2007; Qiu et al. 2007). It is then expected that as a result of null-point reconnection, flare emissions at the footpoints of the fan field lines would constitute a closed circular ribbon flare (CRF), and that the spine-related flare footpoint would be a compact source.

The eruptive filaments, if leaving the corona successfully against the constraining force of the overlying magnetic fields and gravity of the Sun, form the integral part of a CME and its innermost part is identified as core of the CME (Sahu et al. 2020; Mitra et al. 2020; Gopalswamy et al. 2020). CMEs erupt from the lower solar atmosphere and propagate into interplanetary (IP) space through the solar corona with various velocity ranges from hundreds of km s^{-1} to 3000 km s^{-1} (Gopalswamy et al. 2000; Schmieder et al. 2015; Syed Ibrahim et al. 2019; Gopalswamy et al. 2020). In the near-Sun region, it is not completely understood how the magnetic reconnection and geometry/topology of overlying magnetic fields contribute to kinematics of the CMEs (see e.g., Uddin et al. 2012; Joshi et al. 2013; Kushwaha et al. 2015; Joshi et al. 2016; Chandra et al. 2017; Mitra & Joshi 2019; Ravishankar et al. 2020).

The kinematic evolution of CMEs continuously changes from the near-Sun region to near Earth IP medium. Geomagnetic storms are associated with CMEs and their IP counterparts (Zurbuchen & Richardson 2006; Zhao & Dryer 2014; Kilpua et al. 2017; Rubtsov et al. 2018; Bravo et al. 2019; Kharayat et al. 2021). To understand the complex process associated with CME origin and its evolution in the IP medium, it is necessary to connect the near-Sun observations, IP radio emissions and in-situ measurements at 1 AU (see e.g., Joshi et al. 2018). In general, interplanetary coronal mass ejection (ICME) acceleration and deceleration depend on their speed relative to the solar wind speed (Manoharan 2010; Shanmugaraju & Vršnak 2014; Shanmugaraju et al. 2015; Joshi et al. 2018). Slow CMEs are accelerated by the solar wind while fast CMEs are decelerated by the solar wind. Therefore, the transit time of CMEs depends on the state of ambient solar wind condition as well as the CME-CME/CME-solar wind interactions (see, e.g., Manoharan et al. 2004; Manoharan 2006; Vršnak & Žic 2007; Gopalswamy et al. 2015; Syed Ibrahim et al. 2015; Sudar et al. 2016; Syed Ibrahim et al. 2017). Understanding the CME's kinematics and its propagation is very important in the concept of IP space weather. Notably, front-sided Earth directed high speed halo CMEs are potential candidates for major geomagnetic storms. This paper is an attempt to explore the CME initiation and propagation characteristics for a special category of flaring events, called circular ribbon eruptive flares, by utilizing the multi-wavelength and multi-instrumental measurements.

In this study, we discuss two Sun-Earth connecting geoeffective CMEs that erupted on 2013 May 2 and 2014 February 16. The events originated from the ARs NOAA 11731 and 11977 respectively. The source region characteristic of the two events is identical but the subsequent CME evolution shows differences. Hence, it is worthwhile to compare the two events in terms of their near-Sun properties, IP evolution and near-Earth consequences. A very interesting aspect of the source region of these CMEs is their association with impulsive solar eruptive CRFs of similar intensity class (≈M1). Notably, CRFs are generated in ARs that exhibit a particular magnetic topology, known as the fan-spine configuration, which is different from the classical magnetic field configuration of the flaring region where the 'standard' eruptive flares originate (see e.g., Vrsnak 2003; Longcope 2005). The investigations concerning the CME origin and the Sun-Earth connection associated with eruptive CRFs are still very limited; the present study makes inroads toward such objectives. We relied on multi-wavelength and multi-point observations to connect the CME evolution in the near-Sun region to near-Earth space. These solar eruptions lead geomagnetic storms with Dst values from moderate (–20 nT) to intense (–119 nT). In Section 2, we provide details about the various observational resources and data analysis. The characteristics of the flares, CMEs, ICMEs and their interconnection are given in Section 3. The

summary of results and conclusions are stated in the final Section 4.

2 DATA AND SELECTION CRITERION

In this paper, we relied on the following data sources to analyze eruptive flares and CMEs/ICMEs in the Sun-Earth connecting space:

To understand the source region of CMEs, data were obtained from Atmospheric Imaging Assembly (AIA; Lemen et al. 2012) and Helioseismic Magnetic Imager (HMI; Schou et al. 2012) on board the Solar Dynamics Observatory (SDO; Pesnell et al. 2012). We analyzed extreme ultraviolet (EUV) images of the Sun taken in 94 Å, 171 Å, 193 Å and 304 Å filters of AIA which provide useful information about the magnetic loop connectivities, chromospheric features and flare related high-temperature structures. The white light and magnetogram images from HMI provide information about photospheric sunspot evolution and magnetic field of the AR.

We employed the 15 cm f/15 Solar Tower Telescope Hα observations on 2013 May 2 from Aryabhatta Research Institute of Observational Sciences (ARIES) in Nainital, India. The image size was enlarged by a factor of two via a Barlow lens. The images were recorded by a 16 bit 1 k$\times$1 k pixel CCD camera system having a pixel size of 13 μm^2. The cadence for the images is 2–5 s.

A ground based radio spectrograph was employed to study the radio wave mechanism of plasma near-Sun. For this purpose, data were obtained from extended Compound Astronomical Low frequency Low cost Frequency Instrument for Spectroscopy and Transportable Observatory (e-CALLISTO; Benz et al. 2005). Flare details in soft X-ray (SXR) channels are obtained from Geostationary Operational Environmental Satellite (GOES) observations.

To study the CME dynamics in the near-Sun region, we have relied on white light images from the Large Angle and Spectrometric Coronagraph (LASCO; Brueckner et al. 1995) on board Solar and Heliospheric Observatory (SOHO). For understanding CME propagation in IP space, we considered Solar Terrestrial Relations Observatory (STEREO) observations. For ICME tracking, we used data from four instruments: inner coronagraph (COR1), outer coronagraph (COR2) and two heliospheric imagers (HI 1 and 2). Utilizing these instruments one can track the CME/ICME transits from near-Sun to beyond the Earth (Kaiser et al. 2008).

We have analyzed in-situ IP solar wind plasma and magnetic field parameters associated with the CMEs using multi-instrument data which are collectively available at the Coordinated Data Analysis Web (CDAWeb[1]).

3 ANALYSIS AND RESULTS

3.1 Flaring Active Regions NOAA 11731 and 11977 and Source of Circular Ribbon Flares

In Figure 1, we display plots for the evolution of two SXR flares of class M1.1 observed by GOES between 04:58–05:10 UT on 2013 May 2 and 09:20–09:29 UT on 2014 February 16. In these figures, we can see the SXR flux variation in the two different channels (0.5–4 Å and 1–8 Å respectively). The first flaring event, AR NOAA 11731 occurred on 2013 April 24. Initially, the AR displayed a $\beta\gamma\delta$ type magnetic configuration, then four days later it turned into a $\beta\gamma$ type configuration. Then again, it assumed a $\beta\gamma\delta$ configuration on 2013 May 2. The M1.1 class eruptive flare originated on 2013 May 2 when the location of the AR was N10W25.

We present the magnetic configuration of AR NOAA 11731 in Figure 2(a). The white light sunspot image from HMI/SDO clearly indicates the leading part of the AR (see Fig. 2(b)). The distribution of magnetic polarities in the leading part of the AR forms approximately a semicircle which is indicated by the dashed line. There is a small filament that exists at the flaring location in the leading part of the AR which is surrounded by bright plages (see Fig. 2(e)). To compare the photospheric layer with the upper layers, we feature AIA 94 Å and 171 Å images of the AR in panels (c) and (d). Comparisons of the 94 Å and 171 Å filtergram with HMI magnetogram images clearly show that the region of mass eruption and CRF structure extends over the west side of the AR. The filament is connecting the positive and negative polarity of the leading sunspot group. Also the ARIES Hα images clearly elucidate the structure of CRF. In Figure 2(e) and (f), the initial filament, indicated by the red arrow, was observed on 2013 May 2 around 4:59 UT. Filament dark structure and bright foot points are signified by the red arrow and dashed red circle respectively.

The second flaring region NOAA 11977 was visible on the solar disk on 2014 February 10. Initially the AR was a simple α type magnetic configuration, then three days later it turned into a β type configuration. The AR size as well as magnetic complexity developed and changed to a $\beta\gamma$ configuration on 2014 February 14. The intense geoeffective eruptive flare event originated on 2014 February 16 at location S10W00.

Figure 3 shows the multi-wavelength view of the AR NOAA 11977. The sunspot magnetogram and corresponding white light images (Fig. 3(a) and (b)) clearly

[1] https://cdaweb.sci.gsfc.nasa.gov/index.html/

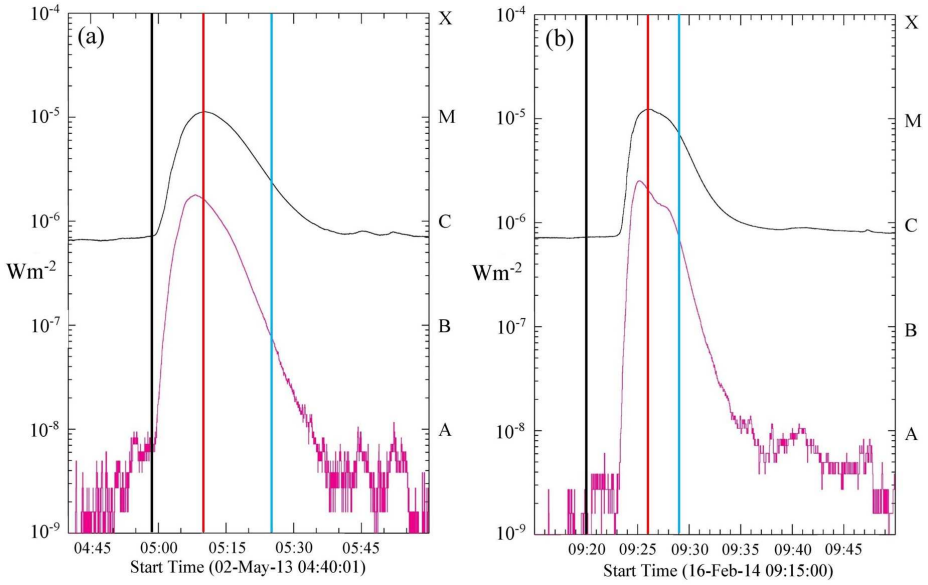

Fig. 1 GOES light curves exhibiting the M1.1 class flare evolution observed on (a) 2013 May 02 04:45–05:45 UT and (b) 2014 February 16 09:18–09:36 UT. Two different wavelengths of 1–8 and 0.5–4 Å correspond to disk-integrated X-ray emission in the 1.5–12.5 keV and 3–25 keV energy ranges, respectively. Vertical solid lines with black, red and green colors indicate the flare start, peak and end times respectively.

indicate the leading and following parts of the AR. The leading sunspot group largely consists of some mixed polarity region at the edge of the AR. A small filament erupted from the complex polarity region and caused the M1.1 impulsive flare and was associated with the moderate speed halo CME. Finally, this CME produced a major geoeffective event. It reached the Earth on 2014 February 19.

During the flare evolution, clearly we can see that the twisted filament erupted from the complex polarity region and it produced CRFs (see Fig. 3(c) and (d)). Colored arrows mark the filament eruption from the merged polarity region (last two panels (e) and (f)). One leg of the filament is anchored on the strong sunspot magnetic field region and another leg is anchored in the weak magnetic field region. The eruption started from the weak field region.

3.2 Radio observations

During these CRFs, the e-CALLISTO spectrograph (Benz et al. 2005) observed emission at radio frequencies. The dynamic solar radio spectra are depicted in Figure 4 at a wide frequency range of 16 to 460 MHz. The dynamic spectrum of the first event displayed a type III burst (Fig. 4(a)). At the peak time of the flare (around 05:05 UT), we observed the type III burst in the frequency range of 150 MHz to 16 MHz. A type III burst implies the opening of the magnetic field lines and subsequent ejection of relativistic electron beam (Joshi et al. 2018). We can see that a type II radio burst is followed by the type III burst. In Figure 4(a), the type II fundamental and harmonic band splitting pattern is indicated by the dashed white and yellow lines respectively. From the metric type II radio observations, we estimate the shock formation height range for upper and lower frequency ranges (120–40 MHz and 46–25 MHz). Corresponding height ranges for the above frequencies are 1.18–1.62 $R_\odot$ and 1.55–1.91 $R_\odot$ (for upper and lower band) respectively. Also the corresponding shock speed is estimated to be 728–835 km s^{-1} using the Newkirk one fold density model (Newkirk 1961a) which is applicable for the lower heights of the solar atmosphere. The average shock speed (782 km s^{-1}) is roughly comparable to the CME speed (671 km s^{-1}) within the LASCO field of view (FOV).

The dynamic radio spectrum of the second flare is given in Figure 4(b). At the peak time of the flare around 09:24 UT, we observed the type III burst between the frequency range of 100 MHz to 45 MHz. There was no type II association, because the flare was associated with a moderate speed CME.

3.3 CME characteristics

The first flare is associated with a moderate speed CME. Figure 5(a) and (b) displays the white-light running difference images from LASCO C2 observations corresponding to the CME observed on 2013 May 2. The CME first appeared at 2.66 $R_\odot$ around 05:24 UT in the C2 FOV, and its linear speed was 671 km s^{-1}. Finally, the

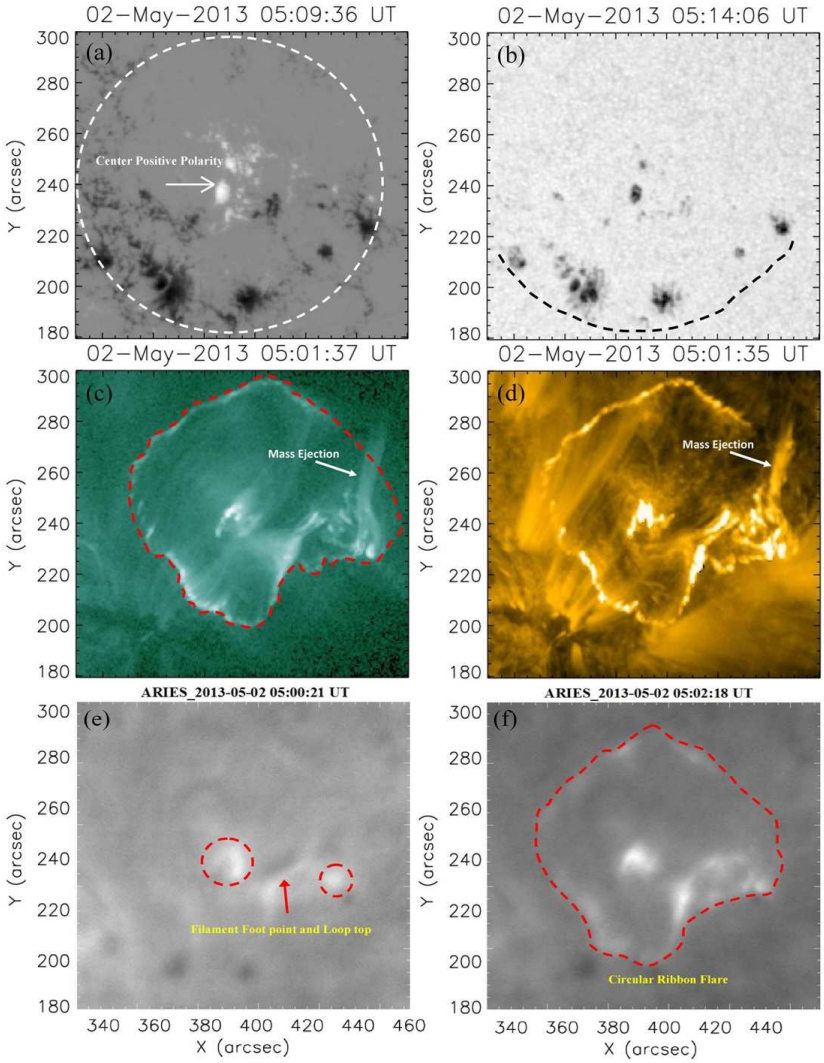

Fig. 2 (a) HMI magnetogram image illustrating the central positive polarity surrounded by a circular type of negative magnetic polarity region which is indicated by the dashed white circle. (b) HMI white light image featuring the sunspot distribution in the AR where semicircular structure in the distribution of sunspots is marked by the dashed line. View of CRF (c) in AIA 94 Å and (d) 171 Å observations. A white arrow indicates the mass eruption from the AR. (e) ARIES solar tower telescope Hα observation for the CRF on 2013 May 2. Filament foot points and loop top are indicated by the dashed red circles and arrow respectively. (f) View of CRF indicated by the dashed red line.

same CME was tracked by the LASCO C3 coronagraph at 21.15 $R_\odot$ around 10:30 UT. The main CME interacted with two pre-CMEs in the LASCO FOV. These two pre-CMEs consecutively erupted around 01:25 UT and 04:24 UT (see Fig. 5(c)). These events were associated with lesser angular widths, and also they propagated in the same direction as the main CME which erupted around 05:24 UT. After the eruption of the main CME, we can see the clear interaction of these events. Central and mean position angles of these three CMEs are nearly the same, around 353 deg.

The second flare is also associated with a moderate speed halo CME. Figure 5(d) and (e) shows the white-light images of the LASCO C2 coronagraph observations on 2014 February 16. CME onset was observed at 2.55 $R_\odot$ around 10:00 UT in the C2 FOV, and its linear speed in the LASCO FOV was 634 km s^{-1}. Finally, the same CME was tracked by the LASCO C3 coronagraph at 6.77 $R_\odot$ around 11:18 UT. This CME event caused an intense storm in the near-Earth environment. Immediately after the main geoeffective CME, a strong bright CME was ejected from the eastern part of the solar limb, so that we cannot track the main geoeffective CME in the LASCO FOV after the distance of 7 $R_\odot$. In the second event, we do not find any evidence of interaction between the pre- and post- CME

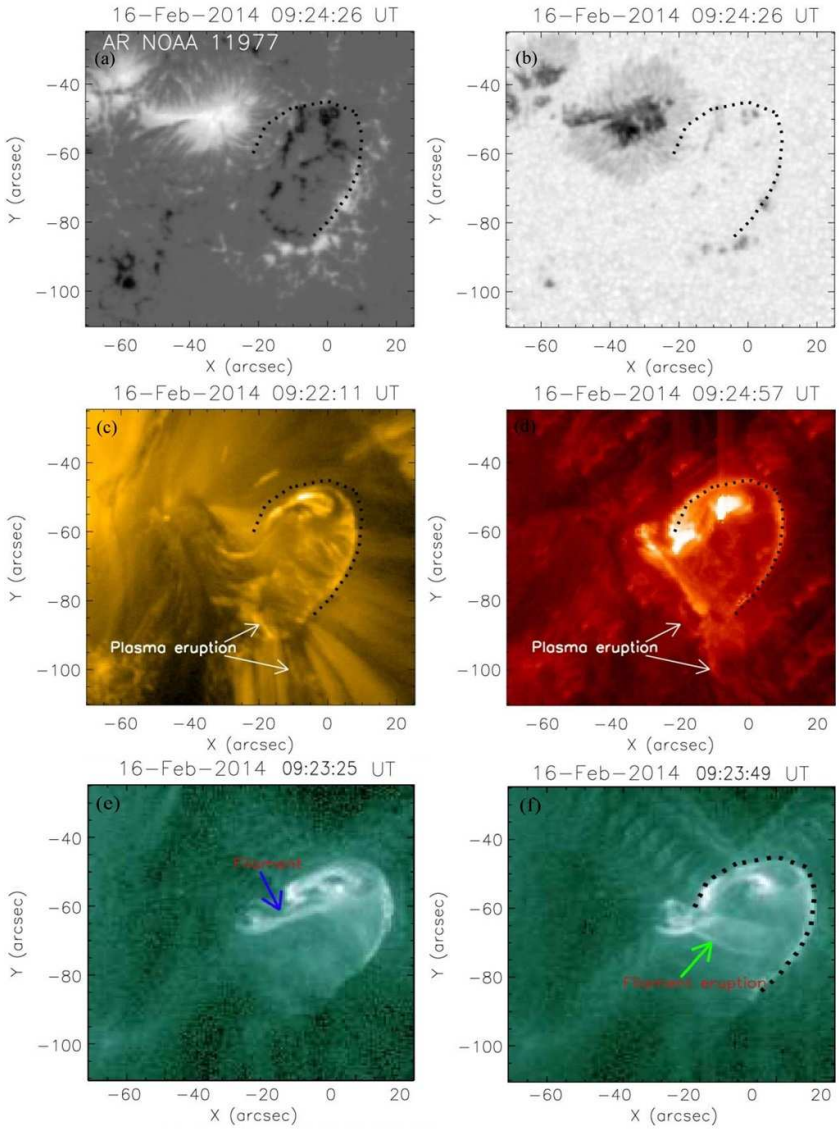

Fig. 3 Multi-wavelength view of AR NOAA 11977 during the flare peak time. (a) HMI magnetogram and (b) white light images are covering the flare region. Circular ribbon flaring region is shown by the dotted curved lines. Circular ribbon flare is visible in AIA observations: (c) 171 Å and (d) 304 Å channels. Filament and its eruption signatures are very clear in the 94 Å observations (see the last two panels (e) and (f)). White arrows indicate the filament eruption/motion. The filament eruption is marked by the colored arrow symbols in the last two panels.

situations. This geoeffective CME was observed by the STEREO coronagraph from Sun to Earth.

Further, we calculated the CME 3D speed relying on STEREO and LASCO observations for both the events. From the graduated cylindrical shell (GCS) model, the obtained speed values for the first and second CMEs are 641 km s^{-1} and 690 km s^{-1}, respectively (Thernisien et al. 2006; Singh et al. 2018).

3.4 EUV waves and direction of CME propagation

The geoeffectiveness of a CME depends upon its direction towards Earth. If the eruption is deflected away from the Earth, it can be less geoeffective. Therefore in this section, we are discussing the direction of CME propagation. Both eruptions are associated with the EUV waves (Fig. 6). Since EUV waves are associated with solar eruptions, deflection in the EUV wave provides information about the deflection of CMEs. Deflections in EUV waves were observed in the past (see e.g., Patsourakos & Vourlidas 2009; Filippov & Srivastava 2010; Zuccarello et al. 2017a; Chandra et al. 2018). The first wave is stronger and clearly associated with a type II radio burst. However, we observed the deflection of this wave. For the second event, we do not find any deflection of the EUV wave and the CME comes directly towards the Earth. From Figure 6, we found that

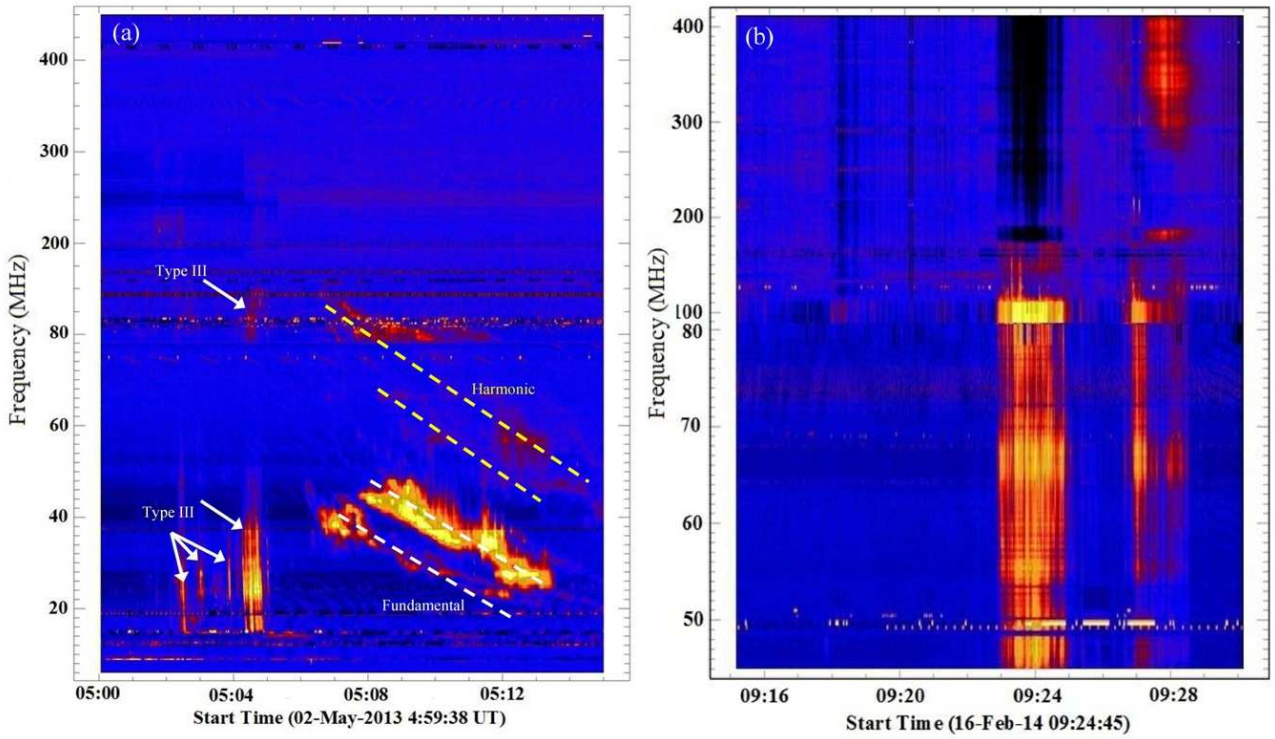

Fig. 4 (a) Dynamic radio spectrum showing the metric type III and type II corresponding to the flare of class M1.1 that occurred on 2013 May 2. Upper and lower type II radio bursts, and fundamental and harmonic frequency band splitting are shown by the dashed white and yellow lines respectively. (b) Dynamic radio spectrum showing metric type III observation corresponding to the class M1.1 flare that occurred on 2014 February 16.

the first CME was deflected from the source region. As we can see, the eruption is not along the radial direction. A huge portion of the CME moved to the north-east part of the Sun (see panels (a), (b), (c) and (d)). Finally, a small part of the CME propagates in IP space. Mostly low-latitude coronal holes appear frequently in the solar disk, so CME deflection by such coronal holes becomes very important (Gopalswamy et al. 2009; Mohamed et al. 2012; Mäkelä et al. 2013). The deflections are thought to be caused by the magnetic pressure gradient between the eruption regions and the coronal holes (Gopalswamy et al. 2001b; Shen et al. 2011; Gui et al. 2011). However, there are other processes that can significantly affect CME propagation, for example CME-CME interaction and CME deflection by large scale structures such as streamers (see e.g., Temmer et al. 2012, 2014; Gopalswamy et al. 2009; Wood et al. 2012; Kay et al. 2013; Panasenco et al. 2013; Gopalswamy & Mäkelä 2014). The deflection angle of the part of the CME's non-radial propagation was much larger than we expect. In most of the reported cases, coronal longitudinal deflections are less than ≈20° (Isavnin et al. 2014) while in this study, we found that the deflection angle of the CME is nearly ≈40°.

Notably, there was no deflection in the case of the second CME, so that most of the CME portion reached the Earth (see Fig. 6(e), (f), (g) and (h)). For the first event, the deflection of CME within the source region is the primary cause for its lower geoeffectiveness (–20 nT). On the other hand, for the second event, the bulk of the CME structure from the source region constituted the corresponding ICMEs and, hence, the event produced strong geoeffectiveness of –119 nT.

3.5 ICME characteristics

Direct evidence of CME propagation and interaction in the IP medium is gathered from STEREO measurements using images from the coronagarph observations (Lugaz et al. 2012). The evolution of the first CME with COR2 images and HI running-difference images is displayed in Figure 7. Examining these snapshot images, we clearly see the CME propagation in the inner and outer heliosphere. CME initial positions are indicated by the black arrow mark in STA COR1 FOV (see Fig. 7(a) and (b)). This particular CME was observed with the STA around 10:24 UT. Further, IP CME propagation is shown in Figure 7(c), (d), (e) and (f) by white arrows.

We constructed an elongation degree map based on the method developed by Sheeley et al. (1999) and Davies et al. (2009). The inclined bright features in the

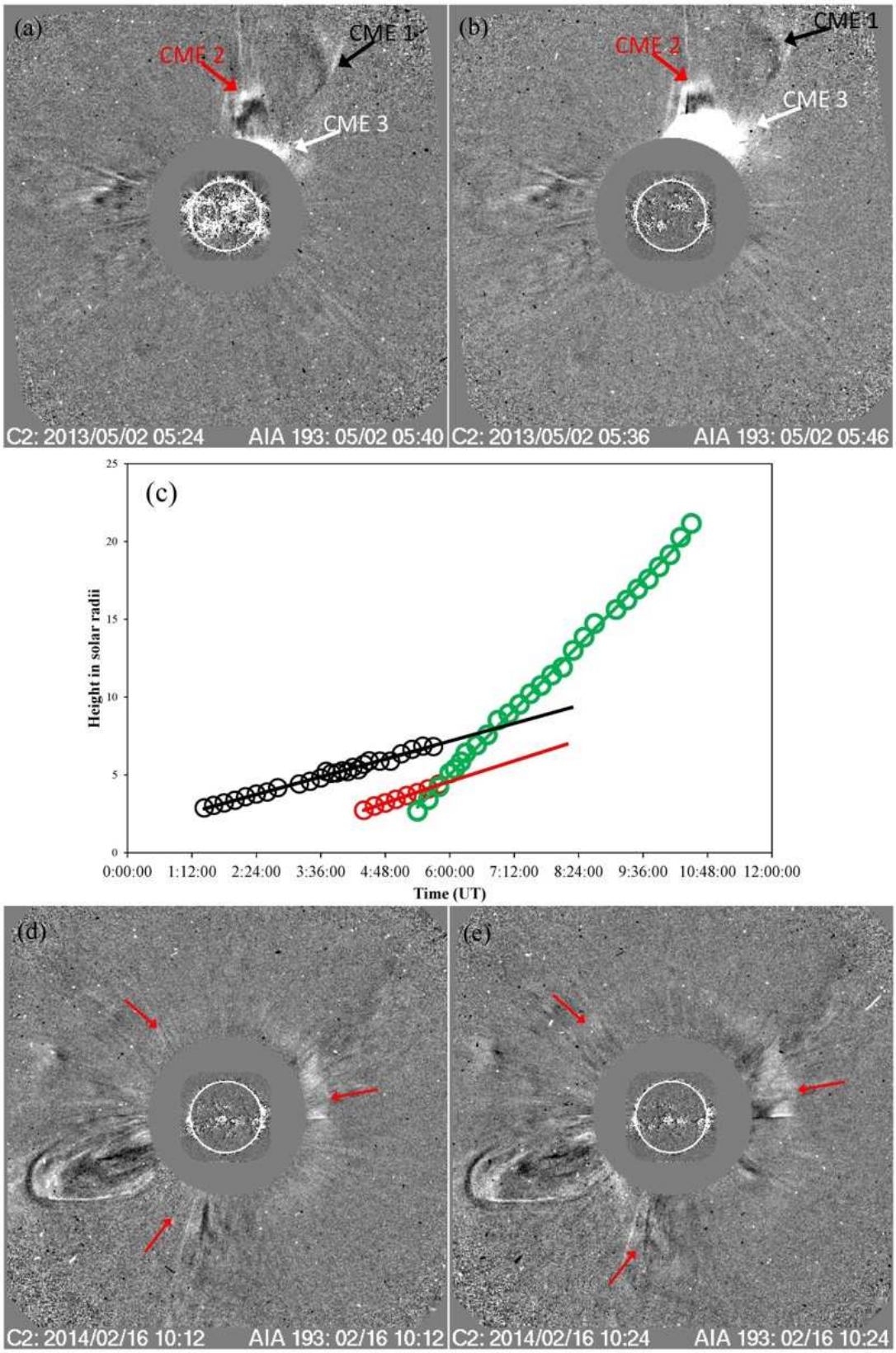

Fig. 5 Running difference images are derived from LASCO C2 observations (panels (a) and (b)) showing the propagation of the moderate speed CME originating from the disk center of AR NOAA 11977 on 2013 May 2. The red and black arrows indicate the two pre-CMEs while the main CME is indicated by a white arrow. (c) The three events interacted in the LASCO FOV. Similarly, the last two panels are displaying the propagation of the halo CME that originated from the AR NOAA 11977 on 2014 February 16. The red colored arrows indicate the halo CME propagation in the LASCO FOV.

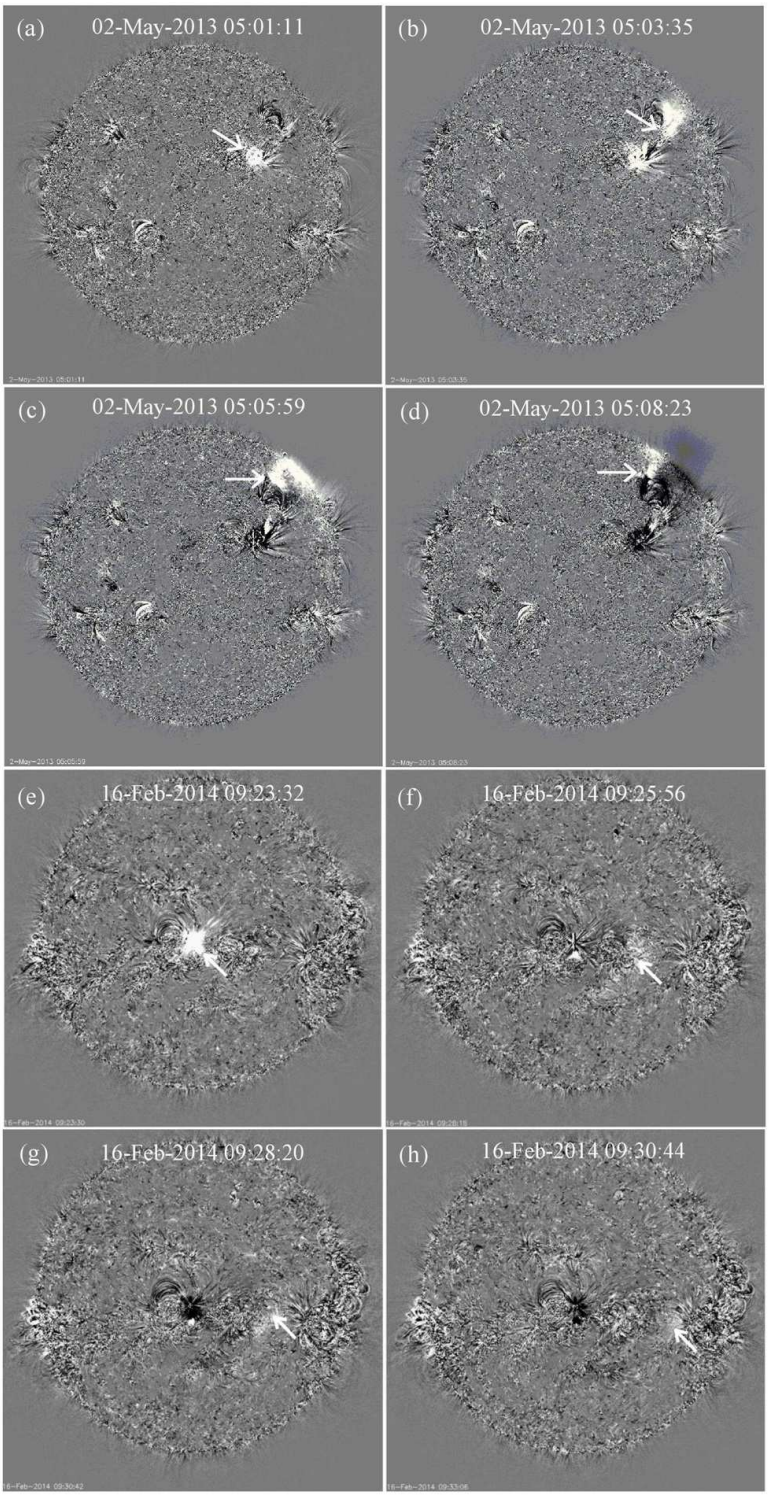

Fig. 6 The first CME event is associated with an EUV wave which is clearly seen in AIA difference images. Importantly, the EUV wave is deflected from the source region. The deflection of the EUV wave is indicated by white arrows (panels (a), (b), (c) and (d)). There was no deflection in the case of an EUV wave associated with the second event (see panels (e), (f), (g) and (h)). The above images are taken from the online available movies (*www.lmsal.com/nitta*).

J-maps (Fig. 7(g)) correspond to the enhanced density structure of the CMEs that erupted during 2013 May 2–8. We tracked the CME/ICME (marked by cross symbols) up to ∼17.50 deg of elongation, equivalent to $\sim 80\,R_{\odot}$. We analyzed CME/ICME height-time information obtained from multi-point and multi-instrument observations. The

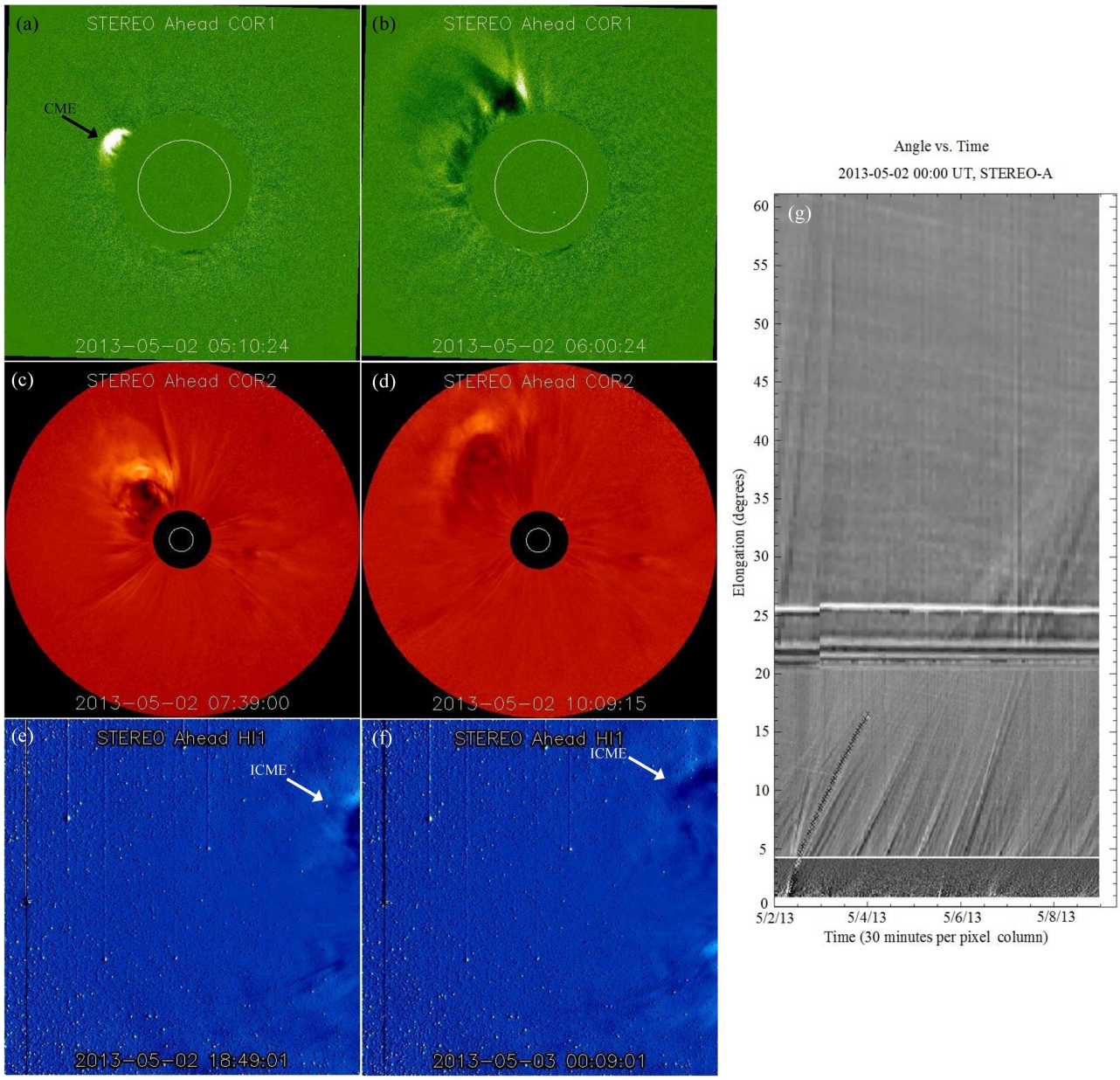

Fig. 7 CME/ICME observation in the STEREO FOV (for the corresponding CME see Fig. 5(a) and (b)). The evolution of the CME in (panels (a) and (b)) COR1 FOV, and the same CME in (panels (c), (d), (e) and (f)) COR2 and HI1 FOV. The propagation of the CME/ICME is clearly visible in the images. A portion of the CME is indicated by the arrows. (g) Time-elongation map (J-map) constructed using the STEREO/SECCHI spacecraft observations during the interval of 2013 May 5 to 8.

calculated CME height (in $R_{\odot}$) and the speed values are plotted in Figure 8(a) and (b). From these figures, we understand that the main CME took approximately 5 d to reach the environment of Earth. The average speed of the CME in the IP medium varied between ∼200 and ∼500 km s^{-1}.

Initial positions of the second event are indicated by the black arrow mark in STA COR1 FOV (see Fig. 9a and b). This particular CME was observed in the STA around 10:09 UT. CME/ICME propagation is displayed in Figure 9(c), (d), (e) and (f) by white arrows. The corresponding J-map is shown in Figure 9(g). We tracked the geoeffective CME (marked by a cross symbol) up to an elongation of ∼50.63 deg, equivalent to ∼228 $R_{\odot}$. The calculated CME height (in $R_{\odot}$) and the speed are given in Figure 10(a) and (b). The second geoeffective CME took approximately 4 d to reach the Earth environment. As noted earlier, this CME produced a major geo-effective event with Dst value

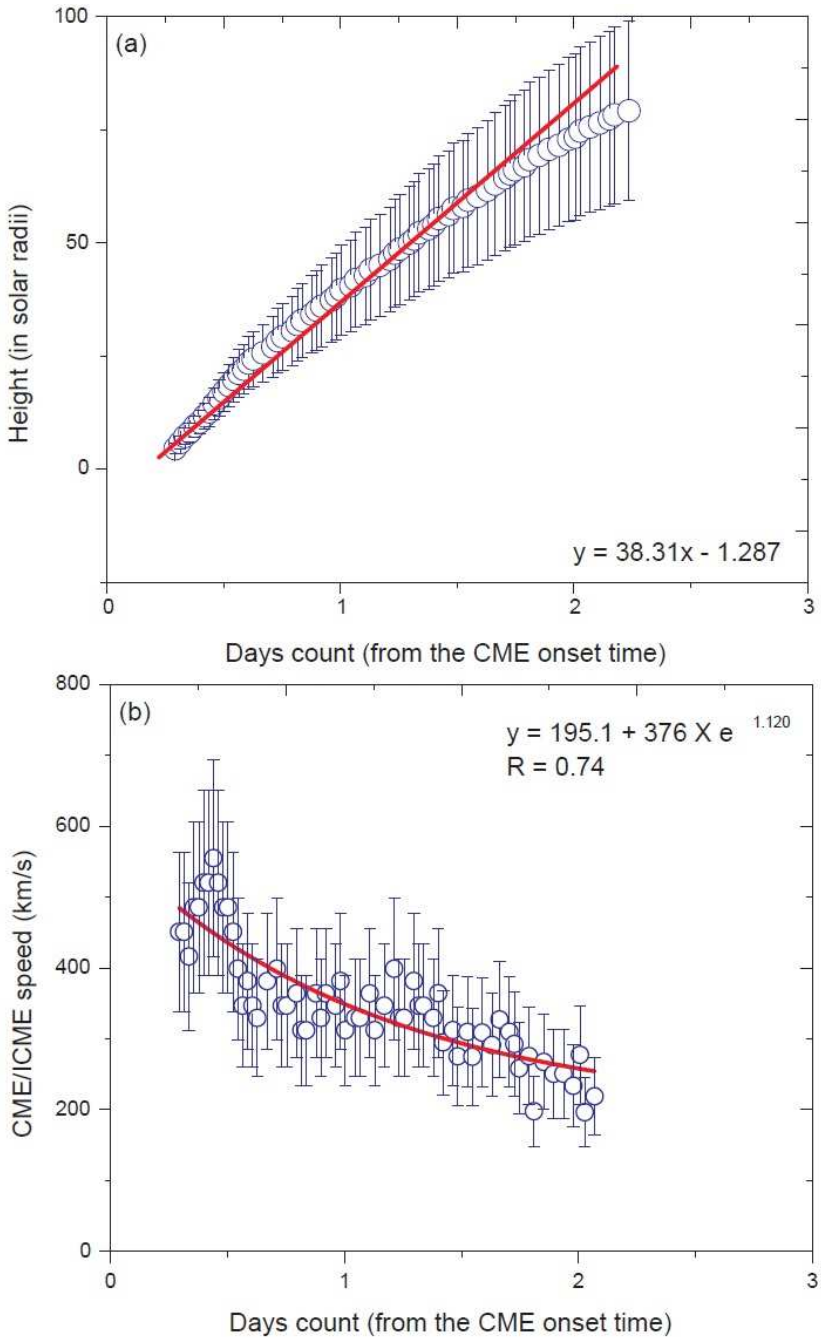

Fig. 8 (a) Obtained CME/ICME height for various times from the STEREO J-map constructions (see Fig. 7(g)). (b) Calculated CME/ICME speed in the STEREO FOV. These figures clearly confirm that the CME/ICME attained the solar wind speed in the IP medium.

of –119 nT. Finally, this CME attains the solar wind speed in the IP medium and its speed ranges between ∼350 and ∼420 km s^{-1}.

3.6 Signature of near Earth ICMEs

We analyzed the in-situ observations taken from the Advanced Composition Explorer (ACE, located at the L1 point) spacecraft to identify the ICME structure. Figure 11 depicts the variation of magnetic field and solar wind plasma parameters from 00:00 UT on 2013 May 5 to 23:59 UT on 2013 May 9. The arrival time of an IP shock is indicated by a sudden enhancement in average magnetic field, Earthward magnetic field components, flow speed, proton density, temperature, and radial component of proton temperature and it was observed at 15:10 UT on 2013 May 5 (marked by the vertical green line). The

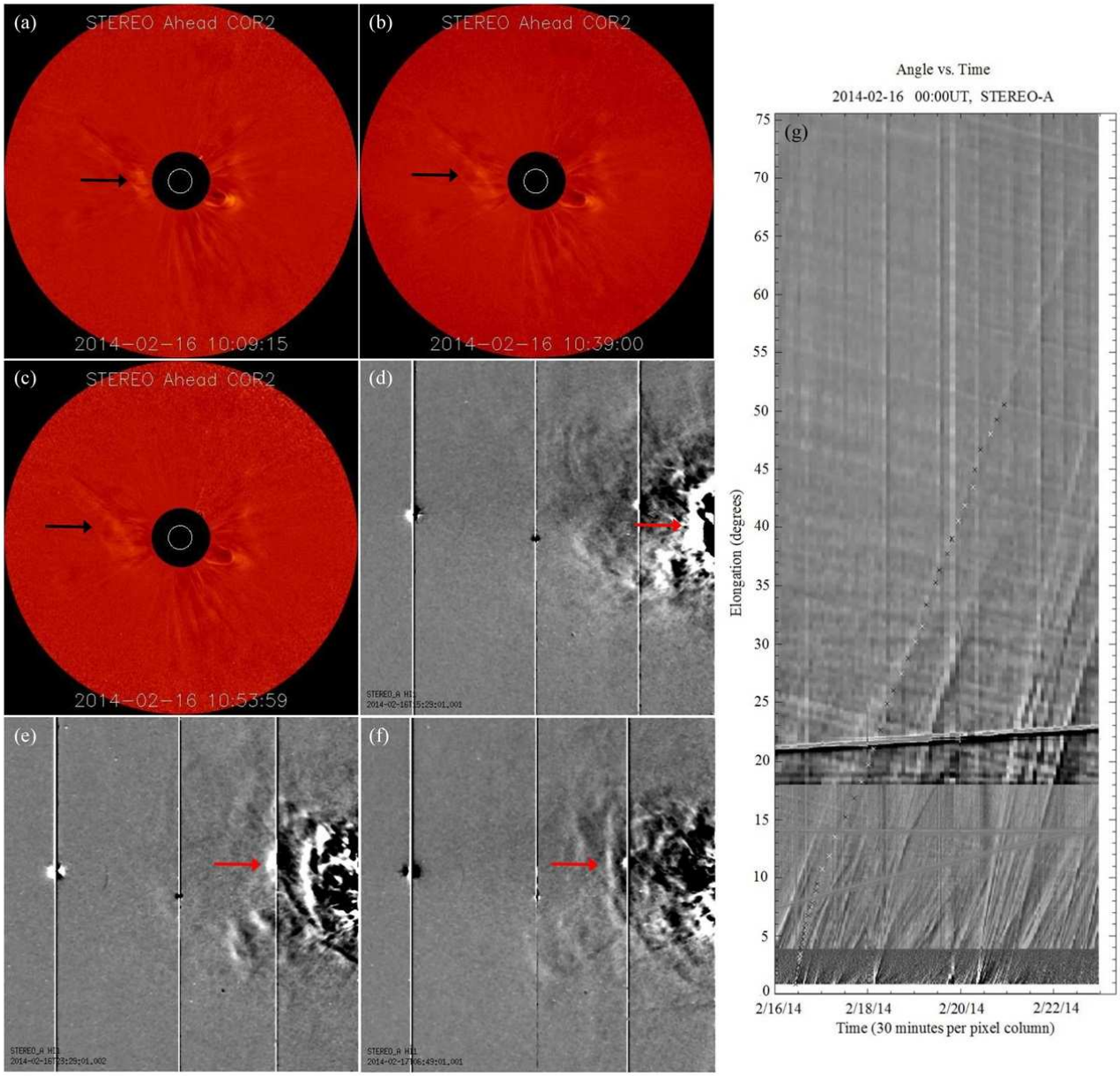

Fig. 9 CME/ICME observation in the STEREO FOV (for the corresponding CME see Fig. 5(d) and (e)). The evolution of the CME in (panels (a), (b) and (c)) COR2 and the same CME in (panels (d), (e) and (f)) HI1 FOV. The propagation of the CME/ICME is indicated by arrows. Time-elongation map (J-map) construction using the STEREO/SECCHI spacecraft observations during the interval of 2014 February 16 to 22.

region between the first and second vertical lines represents the turbulent sheath region. The arrival time of the ICME is indicated by low proton temperature and it is marked by the vertical red line around 16:45 UT on 2013 May 6. The observed arrival times of the IP shock and ICME are 81.77 h and 107.35 hr, respectively. Also, the ICME ending time is marked by the vertical black line. We note a jump in the parameters which are associated with weak IP shock arrival. This weak shock may be related to the flank region of the CME, resulting in an insignificant impact in the near Earth region. Just before the shock arrival, we can see a minor fluctuation in the solar wind parameters which are probably due to a CIR originating from the coronal hole in the solar source regions.

Similarly, second event variations of plasma and magnetic field parameters are given in Figure 12. These parameters were observed from 00:00 UT on 2014 February 18 to 23:59 UT on 2014 February 21. This event is a major geoeffective event and the beginning of storm disturbance is observed at 03:57 UT on 2014 February 19 (marked by the vertical green line). The vertical red line around 12:00 UT on 2014 February 19 indicates the ICME

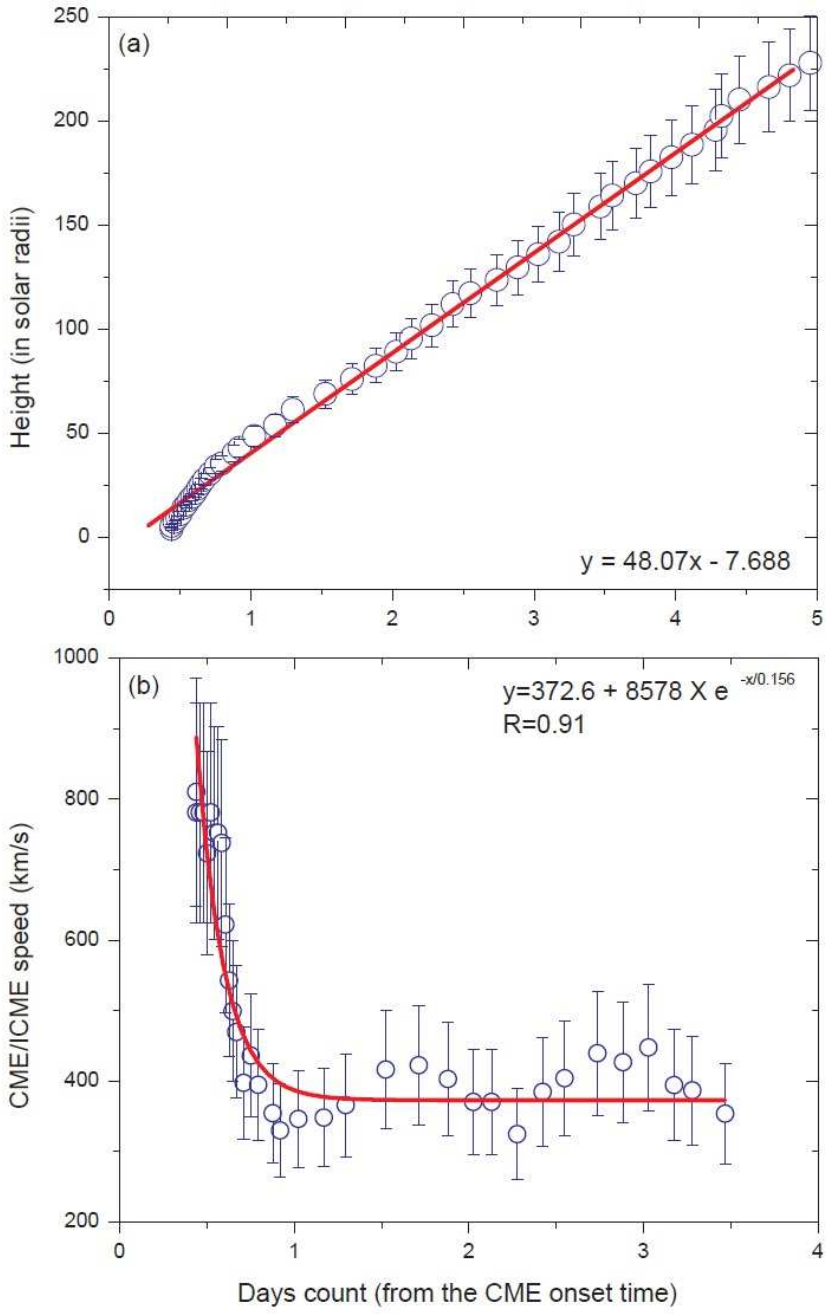

Fig. 10 (a) Obtained CME/ICME height for various times from the STEREO J-map constructions (see Fig. 9(g)). (b) Calculated CME/ICME speed in the STEREO FOV. These figures confirm that the major geoeffective CME/ICME was propagating with a constant speed in the IP medium.

arrival time and the vertical solid black line signifies the ICME ending time. Notably, the SYM/H Dst index is more negative during the interval of passage of the shock sheath region. The Dst index falls to a minimum value of –119 nT at ∼09:00 UT on 2014 February 19. Afterwards, Dst undergoes the recovery phase, but it recovered fully after six days. Before that, the Dst maintained the average value of –50 nT during 2014 February 19–24. The observed arrival times of the IP shock and ICME are 65.95 h and 74.00 h, respectively.

3.7 Estimated Arrival Time using DBM and ESA models

We estimated the arrival time of the ICME/IP shocks at 1 AU employing the following CME/shock prediction model (a) Drag Based Model (DBM) (Vršnak et al.

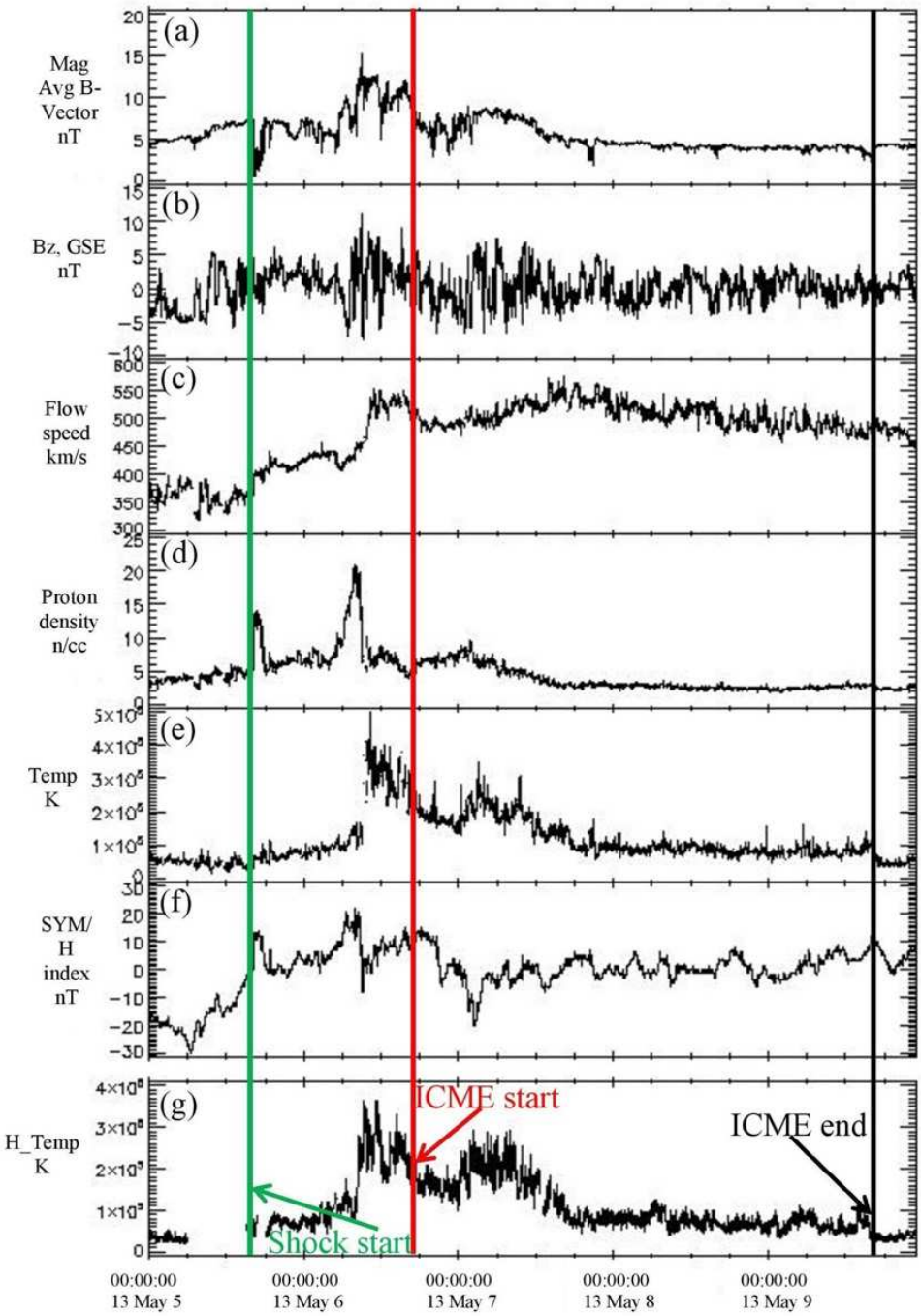

Fig. 11 Near Earth ICME signatures observed at 1 AU by the ACE spacecraft. These in-situ observations of the IP CME correspond to the CME displayed in Fig. 5(a) and (b). The vertical green, red and black lines signify the arrival of the IP shock, and the ICME start and end respectively.

2013), and (b) Empirical Shock Arrival (ESA) model (Gopalswamy et al. 2001a). These models are based on the near-Sun observations of the CME within the SOHO/LASCO FOV. The input parameters of the DBM models are: (1) first observational distance (R_o) of CME, (2) linear speed of the CME, (3) drag parameter (γ) and (4) asymptotic solar wind speed (w). The first observation point of the CME by the C2 coronagraph is at a distance of 2.66 $R_\odot$ at 05:24 UT. Also, the linear speed of the CME in the LASCO FOV is around 671 km s^{-1} and the solar wind speed (obtained from ACE at 1 AU) is around 400 km s^{-1}. Considering these initial input parameters and DBM model, we calculated the CME transit time. The time taken by the CME from its first observation on the Sun to near-Earth is nearly 72.05 h with impact speed (at 1 AU) of 513 km s^{-1}. Further, we calculated the arrival

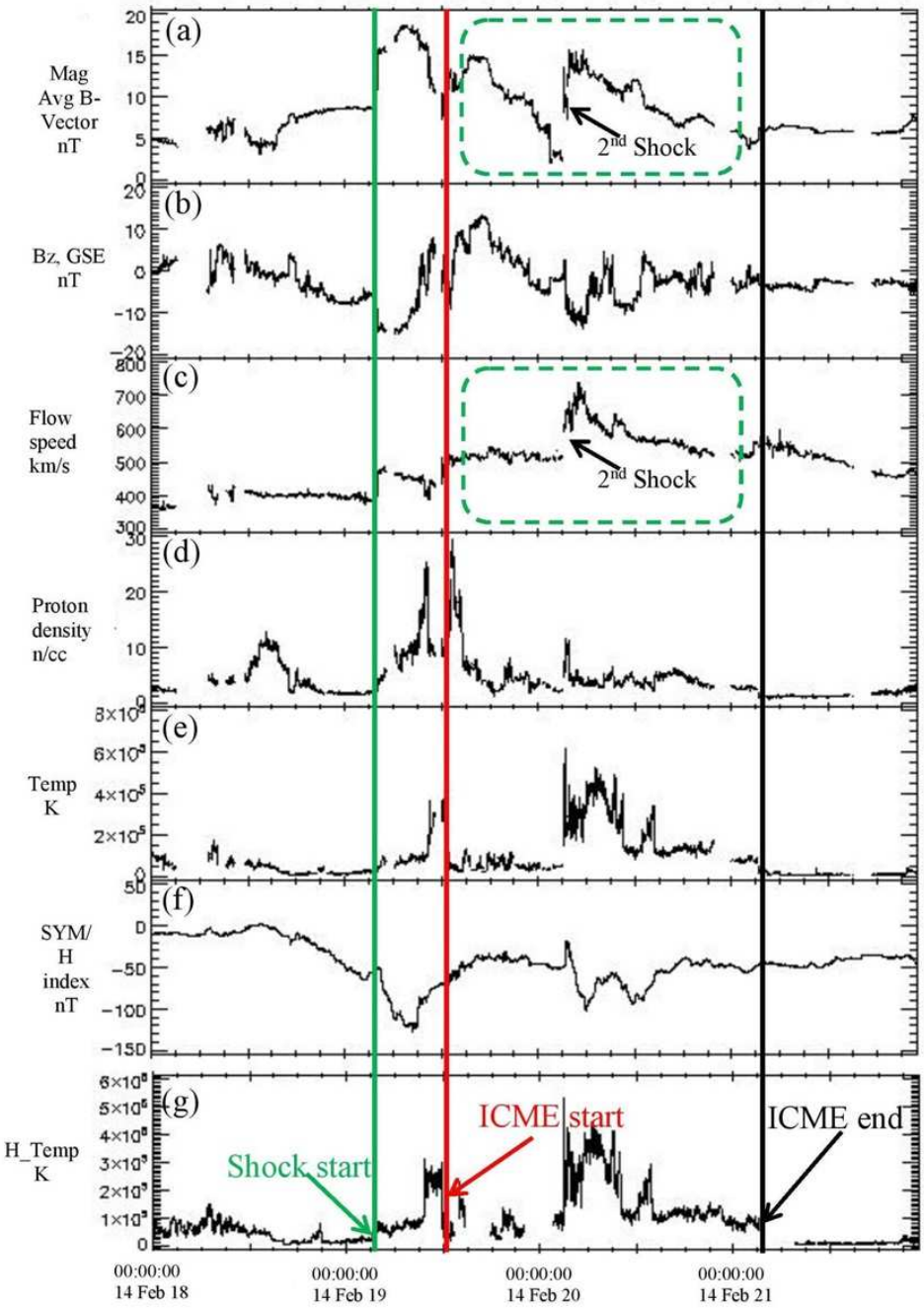

Fig. 12 Near Earth ICME signatures observed at 1 AU by the ACE spacecraft. These in-situ observations of the IP CME correspond to the CME displayed in Fig. 5(d) and (e). The vertical green, red and black lines signify the arrival of the IP shock, and ICME start and end respectively. Interaction region of the ICMEs is marked by the green boxes. Another unknown IP shock is clearly visible in this interaction region.

time of the CME applying the ESA model which is briefly explained in the previous paper (Syed Ibrahim et al. 2015). The estimated arrival time for the IP shock is 84.04 h. Here, we utilized the following acceleration equation a=2.19–(0.0054*CME linear speed) for arrival time which is based on the work of Michałek et al. (2004). A summary of the observations and model predictions is given in Table 1. From this comparison, we also confirm the CME-ICME connection.

The first detection point of the second CME by C2 coronagraph is at a distance of 2.55 $R_{\odot}$ at 10:00 UT. Also, the linear speed of the CME is around 634 km s^{-1} and the solar wind speed is around 400 km s^{-1}. Using the initial parameters and DBM model, we calculated the CME transit time. The time taken by the CME from the

Table 1 Summary of the First CME Initial Observations, along with the Actual and Estimated Transit Times

First observation in LASCO FOV	05:24 UT on 2013 May 2
Height of first observation in LASCO FOV	2.66 $R_{\odot}$
Linear speed (from LASCO FOV observations)	671 km s^{-1}
IP Shock arrival at Near-Earth	∼15:10 UT on 2013 May 5
ICME arrival at Near-Earth	∼16:45 UT on 2013 May 6
Actual transit time for IP shock	
from the first point of the CME observation	81.77 h
Actual Transit time for ICME	
from the first point of the CME observation	107.35 h
Estimated transit time	
from DBM	72.05 h
Estimated transit time	
from ESA model	84.04 h

Table 2 Summary of the CME Initial Observations, along with the Actual and Estimated Transit Times

First observation in LASCO FOV	10:00 UT on 2014 February 16
Height of first observation in LASCO FOV	2.55 $R_{\odot}$
Linear speed (from LASCO FOV observations)	634 km s^{-1}
IP Shock arrival at Near-Earth	∼03:57 UT on 2014 February 19
ICME arrival at Near-Earth	∼12:00 UT on 2014 February 19
Actual transit time for IP shock	
from the first point of the CME observation	65.95 h
Actual Transit time for ICME	
from the first point of the CME observation	74.00 h
Estimated transit time	
from DBM	74.38 h
Estimated transit time	
from ESA model	64.47 h

Sun to near-Earth is nearly 74.38 h with near Earth speed (at 1 AU) of 504 km s^{-1}. Then utilizing the ESA model, we estimated arrival time for the IP shock to be about 64.47 h. Comparison between the observations and model predictions is given in Table 2. From the comparison, we confirm the CME-ICME connection. For both the cases, IP shock arrival shows a good match with the actual observations. In the first case, the prediction error is a little high between the estimated and actual ICME arrival time which could be attributed to the deflection of the erupting structure and/or interaction between the two propagating structures of CME/ICME in the near-Sun region or IP medium.

4 SUMMARY AND CONCLUSIONS

In this article, we have carried out a study of two Earth directed CMEs. We connect and correlate the flare, CME and ICME information from the near-Sun region to the near-Earth environment. In the following, we summarize the important results obtained from the present study.

Both the events clearly show the pre-existence of a small twisted filament associated with the eruptive CRFs. The characteristics of CRF are briefly discussed from multi-channel AIA observations and available Hα images. The formation of circular ribbons at the source regions of both the CMEs indicates that the coronal magnetic field configurations during both events are similar. It is well known that CRFs are associated with a typical fan-spine configuration (see e.g., Devi et al. 2020). Both the CRFs initiated from a complex magnetic field configuration of the AR that exhibits $\beta\gamma$ and $\beta\gamma\delta$ sunspot distributions, respectively, for the first and second event. At the time of flares, the e-CALLISTO radio spectrometer observed a strong type III radio burst. Despite the similarities in the source region configuration and some of the flare characteristics, both CME events produced quite different geoeffective behavior. The first event is also associated with a type II radio burst (Gopalswamy et al. 2001c; Lugaz et al. 2017). Notably, during the first event, we observed CME-CME interactions which were absent during the second event. CME-CME interaction and associated density perturbation increase the probability of type II formation which is likely the case for the first event reported here. From metric type II radio observation and considering the Newkirk density model (Newkirk 1961b), we estimate the shock formation height range of ≈1.18–1.91 $R_{\odot}$ with the corresponding shock speed (782 km s^{-1}).

After eruption of the flares, CMEs were observed in the LASCO C2 FOV with moderate linear speeds of 671 km s^{-1} and 634 km s^{-1} respectively. Further, the CMEs/ICMEs were observed by the STEREO instrument from the Sun to a distance of 1 AU. The in-situ

measurements confirm CME associated IP shocks as well as the ICMEs at 1 AU.

These two CMEs present some similar characteristics, e.g. (i) similar intensity class of associated flare (M1.1), (ii) CRFs and (iii) moderate speed CMEs. However, these events differ in the way of (i) early evolution and propagation of CME during its activation phase in the corona, and (ii) near-Sun pre-post CME interaction. At the near-Earth region, the main difference is that the second event is associated with the major geomagnetic storm with DST ≈–119 nT in comparison to the first event which is associated with the Dst of ≈–20 nT. This is the first detailed study about the geoeffectiveness of CRFs and flare-CME-ICME connections.

The following points are found to be the reasons for the major geoeffectiveness of the second CME:

- While the second CME erupted from the exact disk center of the Sun, the first CME erupted 25° away from the solar disk center. The location of the CME in the solar disk is an important factor that decides its trajectory in the corona and subsequent evolution in the IP medium (Zhang et al. 2003; Manoharan et al. 2004; Dasso et al. 2007; Zhang et al. 2011). Also, when compared to the first event, the second CME was associated with a larger filament eruption (for example see the study by Chandra et al. (2017).
- From the AIA difference images (see Fig. 6), we found that the first eruption is highly deflected from the source AR. Also the eruption direction is not along the radial direction. After the main eruption, a huge part of the CME moved towards the north-east direction of the Sun. The non-radial evolution of the CME as it moves outward from the source AR has been reported in earlier studies (see e.g., Zuccarello et al. 2017a; Mitra et al. 2020). Finally, only a small part of the CME propagates along the Sun-Earth line. Notably, there was no deflection in the case of the second CME, so that most of the CME reached the Earth.
- The first CME seems to be interacting with two pre-CMEs in the LASCO FOV. These two pre-CMEs erupted consecutively around 01:25 UT and 04:24 UT. Very likely, because of the interaction, the first CME might have lost its energy (Gopalswamy et al. 2001c; Yashiro et al. 2014; Shanmugaraju et al. 2014; Joshi et al. 2018; Morosan et al. 2020; Rodríguez Gómez et al. 2020; Scolini et al. 2020).
- Our analysis also suggests that the first event became dissipated in IP space. After a certain distance, the first ICME mingled up with the solar wind.

In summary, the present paper provides detailed multi-wavelength, multi-instrument and multi-point observations of two moderate speed CMEs, both of which were capable of reaching the near-Earth region. The two events seem to be identical in terms of morphology of the associated flare and origin of CME at the source region by filament eruption. The source regions of both the events are also in the central part of the solar disk but within a separation of 25°. However, both CMEs evolve differently beyond the lower coronal region. Our study demonstrates that the CME deflection by the large-scale coronal structures and CME-CME interactions were the major reasons that largely shaped the propagation characteristics of the two events in the upper coronal and IP medium. The present investigation points toward the importance of detecting the changes in the propagation characteristics of the CMEs through a combination of multi-channel and multi-point measurements, such as source region imaging, radio spectral diagnostic, heliospheric imaging and in-situ observations. Understanding the Sun-Earth propagation characteristics of CMEs is a key toward assessing their geoeffective behavior. We plan to analyze the CME observations of a series of circular ribbon eruptive flares in the future.

Acknowledgements We thank the SDO, CALLISTO and GONG teams for their open data policy. We sincerely thank the Aryabhatta Research Institute of Observational Sciences (ARIES) solar observation staffs. We are grateful to the Solar Geophysical Data team, the World Data Center for Geomagnetism (Kyoto University) and the OMNIWeb Plus data and service for their open data policy. The CME catalog used in this study is generated and maintained by the Center for Solar Physics and Space Weather, The Catholic University of America, in cooperation with the Naval Research Laboratory and NASA. The data services from CDAWeb are also thankfully acknowledged.

References

Aulanier, G., Pariat, E., & Démoulin, P. 2005, A&A, 444, 961
Benz, A. O. 2017, Living Reviews in Solar Physics, 14, 2
Benz, A. O., Monstein, C., & Meyer, H. 2005, Sol. Phys., 226, 143
Bravo, M. A., Batista, I. S., Souza, J. R., & Foppiano, A. J. 2019, Journal of Geophysical Research (Space Physics), 124, 9405
Brueckner, G. E., Howard, R. A., Koomen, M. J., et al. 1995, Sol. Phys., 162, 357
Carmichael, H. 1964, A Process for Flares, 50, NASA Special Publication, 50 (Washington, DC: National Aeronautics and Space Administration, Science and Technical Information Division), 451
Chandra, R., Chen, P. F., Joshi, R., et al. 2018, ApJ, 863, 101

Chandra, R., Filippov, B., Joshi, R., & Schmieder, B. 2017, Sol. Phys., 292, 81
Dasso, S., Nakwacki, M. S., Démoulin, P., & Mandrini, C. H. 2007, Sol. Phys., 244, 115
Davies, J. A., Harrison, R. A., Rouillard, A. P., et al. 2009, Geophys. Res. Lett., 36, L02102
Demoulin, P., Bagala, L. G., Mandrini, C. H., et al. 1997, A&A, 325, 305
Demoulin, P., Henoux, J. C., Priest, E. R., & Mandrini, C. H. 1996, A&A, 308, 643
Démoulin, P., Hénoux, J. C., Schmieder, B., et al. 1994, Space Sci. Rev., 68, 129
Devi, P., Joshi, B., Chandra, R., et al. 2020, Sol. Phys., 295, 75
Filippov, B., & Srivastava, A. K. 2010, Sol. Phys., 266, 123
Gibson, S. E., & Fan, Y. 2006, Journal of Geophysical Research (Space Physics), 111, A12103
Gopalswamy, N., Akiyama, S., Yashiro, S., et al. 2020, in Journal of Physics Conference Series, 1620, 012005
Gopalswamy, N., Lara, A., Lepping, R. P., et al. 2000, Geophys. Res. Lett., 27, 145
Gopalswamy, N., Lara, A., Yashiro, S., et al. 2001a, J. Geophys. Res., 106, 29207
Gopalswamy, N., & Mäkelä, P. 2014, in Astronomical Society of the Pacific Conference Series, 484, Outstanding Problems in Heliophysics: From Coronal Heating to the Edge of the Heliosphere, eds. Q. Hu, & G. P. Zank, 63
Gopalswamy, N., Mäkelä, P., Xie, H., et al. 2009, Journal of Geophysical Research (Space Physics), 114, A00A22
Gopalswamy, N., Yashiro, S., Kaiser, M. L., et al. 2001b, ApJL, 548, L91
Gopalswamy, N., Yashiro, S., Kaiser, M. L., et al. 2001c, ApJL, 548, L91
Gopalswamy, N., Yashiro, S., Xie, H., et al. 2015, Journal of Geophysical Research (Space Physics), 120, 9221
Gui, B., Shen, C., Wang, Y., et al. 2011, Sol. Phys., 271, 111
Hirayama, T. 1974, Sol. Phys., 34, 323
Hudson, H. S. 2011, Space Sci. Rev., 158, 5
Isavnin, A., Vourlidas, A., & Kilpua, E. K. J. 2014, Sol. Phys., 289, 2141
Janvier, M., Savcheva, A., Pariat, E., et al. 2016, A&A, 591, A141
Joshi, B., Ibrahim, M. S., Shanmugaraju, A., & Chakrabarty, D. 2018, Sol. Phys., 293, 107
Joshi, B., Kushwaha, U., Cho, K. S., & Veronig, A. M. 2013, ApJ, 771, 1
Joshi, B., Kushwaha, U., Veronig, A. M., & Cho, K. S. 2016, ApJ, 832, 130
Joshi, B., Kushwaha, U., Veronig, A. M., et al. 2017a, ApJ, 834, 42
Joshi, B., Thalmann, J. K., Mitra, P. K., et al. 2017b, ApJ, 851, 29
Joshi, B., Veronig, A., Manoharan, P. K., & Somov, B. V. 2012, Astrophysics and Space Science Proceedings, 33, 29
Joshi, N. C., Liu, C., Sun, X., et al. 2015, ApJ, 812, 50
Kaiser, M. L., Kucera, T. A., Davila, J. M., et al. 2008, Space Sci. Rev., 136, 5
Kay, C., Opher, M., & Evans, R. M. 2013, ApJ, 775, 5
Kharayat, H., Joshi, B., & Chandra, R. 2021, Ap&SS, 366, 24
Kilpua, E. K. J., Balogh, A., von Steiger, R., & Liu, Y. D. 2017, Space Sci. Rev., 212, 1271
Kopp, R. A., & Pneuman, G. W. 1976, Sol. Phys., 50, 85
Krall, J., & Sterling, A. C. 2007, ApJ, 663, 1354
Kushwaha, U., Joshi, B., Cho, K.-S., et al. 2014, ApJ, 791, 23
Kushwaha, U., Joshi, B., Veronig, A. M., & Moon, Y.-J. 2015, ApJ, 807, 101
Lau, Y.-T., & Finn, J. M. 1990, ApJ, 350, 672
Lemen, J. R., Title, A. M., Akin, D. J., et al. 2012, Sol. Phys., 275, 17
Li, Y., Qiu, J., Longcope, D. W., Ding, M. D., & Yang, K. 2016, ApJL, 823, L13
Liu, C., Prasad, A., Lee, J., & Wang, H. 2020, ApJ, 899, 34
Longcope, D. W. 2005, Living Reviews in Solar Physics, 2, 7
Lugaz, N., Farrugia, C. J., Davies, J. A., et al. 2012, ApJ, 759, 68
Lugaz, N., Temmer, M., Wang, Y., & Farrugia, C. J. 2017, Sol. Phys., 292, 64
Mäkelä, P., Gopalswamy, N., Xie, H., et al. 2013, Sol. Phys., 284, 59
Manoharan, P. K. 2006, Sol. Phys., 235, 345
Manoharan, P. K. 2010, Sol. Phys., 265, 137
Manoharan, P. K., Gopalswamy, N., Yashiro, S., et al. 2004, Journal of Geophysical Research (Space Physics), 109, A06109
Masson, S., Pariat, E., Aulanier, G., & Schrijver, C. J. 2009, ApJ, 700, 559
Michałek, G., Gopalswamy, N., Lara, A., & Manoharan, P. K. 2004, A&A, 423, 729
Mitra, P. K., & Joshi, B. 2019, ApJ, 884, 46
Mitra, P. K., Joshi, B., Prasad, A., et al. 2018, ApJ, 869, 69
Mitra, P. K., Joshi, B., Veronig, A. M., et al. 2020, ApJ, 900, 23
Mohamed, A. A., Gopalswamy, N., Yashiro, S., et al. 2012, Journal of Geophysical Research (Space Physics), 117, A01103
Morosan, D. E., Palmerio, E., Räsänen, J. E., et al. 2020, A&A, 642, A151
Newkirk, Gordon, J. 1961a, ApJ, 133, 983
Newkirk, Gordon, J. 1961b, ApJ, 133, 983
Panasenco, O., Martin, S. F., Velli, M., & Vourlidas, A. 2013, Sol. Phys., 287, 391
Patsourakos, S., & Vourlidas, A. 2009, ApJL, 700, L182
Pesnell, W. D., Thompson, B. J., & Chamberlin, P. C. 2012, Sol. Phys., 275, 3
Pontin, D. I., Bhattacharjee, A., & Galsgaard, K. 2007, Physics of Plasmas, 14, 052106
Pontin, D. I., & Galsgaard, K. 2007, Journal of Geophysical Research (Space Physics), 112, A03103
Qiu, J., Hu, Q., Howard, T. A., & Yurchyshyn, V. B. 2007, ApJ,

659, 758
Ravishankar, A., Michałek, G., & Yashiro, S. 2020, A&A, 639, A68
Reid, H. A. S., Vilmer, N., Aulanier, G., & Pariat, E. 2012, A&A, 547, A52
Rodríguez Gómez, J. M., Podladchikova, T., Veronig, A., et al. 2020, ApJ, 899, 47
Rubtsov, A. V., Agapitov, O. V., Mager, P. N., et al. 2018, Journal of Geophysical Research (Space Physics), 123, 9406
Sahu, S., Joshi, B., Mitra, P. K., et al. 2020, ApJ, 897, 157
Schmieder, B., Aulanier, G., & Vršnak, B. 2015, Sol. Phys., 290, 3457
Schou, J., Scherrer, P. H., Bush, R. I., et al. 2012, Sol. Phys., 275, 229
Scolini, C., Chané, E., Temmer, M., et al. 2020, ApJS, 247, 21
Shanmugaraju, A., Prasanna Subramanian, S., Vrsnak, B., & Ibrahim, M. S. 2014, Sol. Phys., 289, 4621
Shanmugaraju, A., Syed Ibrahim, M., Moon, Y. J., et al. 2015, Sol. Phys., 290, 1417
Shanmugaraju, A., & Vršnak, B. 2014, Sol. Phys., 289, 339
Sheeley, N. R., Walters, J. H., Wang, Y. M., & Howard, R. A. 1999, J. Geophys. Res., 104, 24739
Shen, C., Wang, Y., Gui, B., et al. 2011, Sol. Phys., 269, 389
Shibata, K. 1999, Ap&SS, 264, 129
Singh, T., Yalim, M. S., & Pogorelov, N. V. 2018, ApJ, 864, 18
Sturrock, P. A. 1966, Nature, 211, 695
Sudar, D., Vršnak, B., & Dumbović, M. 2016, MNRAS, 456, 1542
Syed Ibrahim, M., Joshi, B., Cho, K. S., et al. 2019, Sol. Phys., 294, 54
Syed Ibrahim, M., Manoharan, P. K., & Shanmugaraju, A. 2017, Sol. Phys., 292, 133
Syed Ibrahim, M., Shanmugaraju, A., & Bendict Lawrance, M. 2015, Advances in Space Research, 55, 407
Temmer, M., Veronig, A. M., Peinhart, V., & Vršnak, B. 2014, ApJ, 785, 85
Temmer, M., Vršnak, B., Rollett, T., et al. 2012, ApJ, 749, 57
Thernisien, A. F. R., Howard, R. A., & Vourlidas, A. 2006, ApJ, 652, 763
Toriumi, S., & Wang, H. 2019, Living Reviews in Solar Physics, 16, 3
Uddin, W., Schmieder, B., Chandra, R., et al. 2012, ApJ, 752, 70
Vrsnak, B. 2003, Magnetic 3-D Configurations of Energy Release in Solar Flares, ed. L. Klein, 612, Energy Conversion and Particle Acceleration in the Solar Corona (Lecture Notes in Physics), 28
Vršnak, B., & Žic, T. 2007, A&A, 472, 937
Vršnak, B., Žic, T., Vrbanec, D., et al. 2013, Sol. Phys., 285, 295
Wood, B. E., Wu, C. C., Rouillard, A. P., Howard, R. A., & Socker, D. G. 2012, ApJ, 755, 43
Yashiro, S., Gopalswamy, N., Mäkelä, P., et al. 2014, Advances in Space Research, 54, 1941
Zhang, H.-Q., Bao, X.-M., Zhang, Y., et al. 2003, ChJAA (Chin. J. Astron. Astrophys.), 3, 491
Zhang, Y. Z., Feng, X. S., & Song, W. B. 2011, ApJ, 728, 21
Zhao, X., & Dryer, M. 2014, Space Weather, 12, 448
Zhong, Z., Guo, Y., Ding, M. D., Fang, C., & Hao, Q. 2019, ApJ, 871, 105
Zuccarello, F. P., Chandra, R., Schmieder, B., et al. 2017a, A&A, 601, A26
Zurbuchen, T. H., & Richardson, I. G. 2006, Space Sci. Rev., 123, 31